

Received:  
27 March 2017  
Revised:  
7 June 2017  
Accepted:  
28 July 2017

Cite as: A-F. Obaton, J. Fain, M. Djemai, D. Meinel, F. Léonard, E. Mahé, B. Lécuelle, J-J. Fouchet, G. Bruno. *In vivo* XCT bone characterization of lattice structured implants fabricated by additive manufacturing. *Heliyon* 3 (2017) e00374. doi: 10.1016/j.heliyon.2017.e00374



# *In vivo* XCT bone characterization of lattice structured implants fabricated by additive manufacturing

A-F. Obaton<sup>a,\*</sup>, J. Fain<sup>b</sup>, M. Djemai<sup>b</sup>, D. Meinel<sup>c</sup>, F. Léonard<sup>c</sup>, E. Mahé<sup>a</sup>, B. Lécuelle<sup>d</sup>, J-J. Fouchet<sup>b</sup>, G. Bruno<sup>c</sup>

<sup>a</sup> LNE, Laboratoire commun de métrologie (LNE/Cnam), Laboratoire National de Métrologie et d'Essais (LNE), 1 rue Gaston Boissier, Paris 75015, France

<sup>b</sup> Z3Dlab, Parc Technologique, 26 Rue des Sablons, Montmagny 95360, France

<sup>c</sup> BAM, 8.5 – Micro-NDT, Unter den Eichen 87, Berlin 12205, Germany

<sup>d</sup> Ecole Nationale Vétérinaire d'Alfort, Centre de Recherche BioMédicale, 7, av. du Général de Gaulle, Maisons-Alfort 94704, France

\* Corresponding author.

E-mail address: [anne-francoise.obaton@lne.fr](mailto:anne-francoise.obaton@lne.fr) (A.-F. Obaton).

## Abstract

Several cylindrical specimens and dental implants, presenting diagonal lattice structures with different cell sizes (600, 900 and 1200  $\mu\text{m}$ ) were additively manufactured by selective laser melting process. Then they were implanted for two months in a sheep. After removal, they were studied by Archimedes' method as well as X-ray computed tomography in order to assess the penetration of bone into the lattice. We observed that the additive manufactured parts were geometrically conformed to the theoretical specifications. However, several particles were left adhering to the surface of the lattice, thereby partly or entirely obstructing the cells. Nevertheless, bone penetration was clearly visible. We conclude that the 900  $\mu\text{m}$  lattice cell size is more favourable to bone penetration than the 1200  $\mu\text{m}$  lattice cell size, as the bone penetration is 84% for 900  $\mu\text{m}$  against 54% for 1200  $\mu\text{m}$  cell structures. The lower bone penetration value for the 1200  $\mu\text{m}$  lattice cell could possibly be attributed to the short residence time in the sheep. Our results lead to the

conclusion that lattice implants additively manufactured by selective laser melting enable better bone integration.

**Keywords:** Biomedical engineering, Dentistry, Medical imaging, Bioengineering, Materials science

## 1. Introduction

Additive manufacturing (AM) is spreading out in industry for two main reasons. The first one, is that AM offers the possibility to effectively manufacture very complex parts, in particular lattice structures, which would not be easily fabricated with conventional methods. The second one is that AM offers to manufacture, on demand, customised parts. These two reasons are of particular interest for the medical sector. Indeed, the lattice structures considerably increase the contact zones between the bone and the implant and thus can lead to better fixation of the implant if the lattice is colonized in depth. This adaptation to the forms is the first element of implant-bone cohesion. Also, osteo-integration of AM implants is better than machined implants because of the surface roughness of AM parts that favours the attachment of bone [1, 2, 3]. Besides their adaptability to complex structures, such parts are considerably less expensive than their analogs produced by subtractive methods or casting. On another hand, on demand customised medical devices reduce the need of a large inventory of different sizes of sterile storage. Thus these key advantages provide customised complex implants which match the patient's anatomy [4] and thus reduce the recovery time of the patient after surgery. They can be used for specialities such as orthopaedic, spinal, cranial, maxillo-facial, and dental surgery.

There are several AM processes. The International Organization for Standardization (ISO) [5] classified them into seven categories: 1) vat photopolymerization; 2) material jetting; 3) material extrusion; 4) binder jetting; 5) powder bed fusion; 6) directed energy deposition; 7) sheet lamination. The first three process categories consist of the selective solidification of a resin or of a hot melt material (mainly polymer or ceramic filled polymer); the following three categories, concern the selective conglomeration or fusion of powder (mainly polymer, ceramic and metal); and the last one refers to the bonding of sheet materials (mainly paper, cardboard and wood). The metallic AM category of process that is predominately used in the medical sector is powder bed fusion. This category of process uses thermal energy to selectively fuse regions of a powder bed. The thermal source of activation can be mostly an electron beam (EBM for electron beam melting) or a laser (SLM for selective laser melting).

It is commonplace to say, in the AM community, that lattice structures enable better bone growth which also contributes to the reduction of the patient recovery

time. However, this last assumption has not been rigorously validated. The penetration of bone into the cells of the lattice structures have to be highlighted.

We are proposing, in this paper, the analysis of SLM titanium lattice structures of different cell sizes implanted in the legs of a sheep for two months, and the usability of industrial X-ray computed tomography (XCT) to highlight the penetration of bone into these lattice structures. We are also comparing the XCT scan to the numerical model of the lattice structure (Computer-aided design, CAD) to check the compliance with specifications. This study has an exploratory nature, and precedes any further development of art. Our focus lies in the material-bone integration, and stands before any medical study that would include statistical analysis, as well would target specific applications.

XCT is a volumetric 3D imaging technique which enables to go deeply inside the matter. It involves two main steps: 1) a step where the relative loss of the X-ray radiation intensity, after it has passed through the sample under test, is measured at different angles; followed by one purely mathematical 2) step where the inverse problem is resolved with specific algorithms to numerically digitally reconstruct the sample in 3D. The resulting 3D images are grayscale images that show the local linear attenuation coefficient throughout the sample. Unlike histology studies which are invasive and need several manipulations, XCT is a volumetric non-invasive technique.

Dense AM implants without lattice, as well as just with the surface covered with lattices are already proposed in the literature. For example, implants developed by Zimmer, are dense titanium implants covered by lattice tantalum structure [6, 7]. However, the lattice structures have limited penetration in the titanium surface. Moreover, Ta is much less suited as a material for implants because of its costs, its scarcity and is difficult to work with. On another side, Palmquist et al. [8] and Guoyan Li et al. [9] have proposed similar study to what we are proposing but for EBM implants. However, the powder size used in EBM (80–100  $\mu\text{m}$ ) is much larger than the one used in SLM (20–50  $\mu\text{m}$ ). Consequently, the roughness is higher and the spatial resolution is lower in EBM, which make the bone penetration different in EBM and SLM implants. So, to our knowledge, this is the first time that such study is carried out for SLM implants.

Our paper is divided into four parts. In the first part, the materials will be addressed. The material model, the implants and two different characterisation techniques will be presented. These two techniques are Archimedes' method for density measurement and XCT for volumetric non-destructive 3D imaging. In the second part, the methods as well as the protocols followed regarding the material will be described. In the third part, the results will be displayed, and in the fourth part the results will be discussed.

## 2. Materials

### 2.1. Animal model

Only one female sheep was involved in this exploratory study to highlight bone integration inside lattice structures. The animal was a five years old adult (53.6 kg) bred by the French institute for agronomical research (Institut National de Recherche Agronomique-INRA-). Two tibias were used for the inclusion of all the implants.

The two days immediately following surgery excluded, where the sheep was housed in individual pens with eye contact with their companions, then a group of sheep were housed during the whole study. They were supplied with vegetal bedding, *ad libitum* hay and water. Temperature was maintained between 19 and 22 °C and animals were exposed to an artificial 12L–12 G light cycle. A daily check of their physical condition was performed throughout the study.

### 2.2. Implants

Two shapes of specimens were introduced into the sheep, both fabricated by additive manufacturing of titanium (Ti6Al4 V grade 23) by the French company Z3DLab: conical threaded dental implants with inside lattice structure and cylindrical lattice bone generic implants. The purpose of the work is to identify bone penetration inside lattice structures using X-ray tomography, so the outer geometry of the parts played a less important role than the inner features (lattice structure).

#### 2.2.1. Dental implants

The shape of the dental implants [10] was conical with a 10 mm height, a 4 mm diameter at largest and a 3° slope (Fig. 1). Three millimetres from the larger end, a thread of metric type was presented, with a pitch of 0.8 mm and depths of 0.34 mm.



**Fig. 1.** Photograph of the studied dental implant [10].

The larger end of the cone had a hexagonal cavity of 2 mm in size and 2.2 mm in depth, to screw the implant into the bone. The implants had an internal DNA shape lattice structure. The lattice was either diamond or diagonal shaped with 600, 900 or 1200  $\mu\text{m}$  cell (i.e. cavity) sizes.

### 2.2.2. Cylindrical specimens

The height of the cylindrical specimens was 10 mm, with a 6 mm diameter separated in the middle by vertical and horizontal partitions (Fig. 2). A lattice structure of diagonal cells constituted the upper zones whereas diamond cells constitute the lower zones. The sizes of the lattice cells were 600, 900 or 1200  $\mu\text{m}$ . The top and bottom of the cylinder are closed by dense surfaces. In this way, the bone penetration is peripherally limited.

None of these samples underwent heat treatment or polishing. However the following cleaning protocol was applied:

- 60 min in an ultrasound tank with 60 °C distilled water without any detergent;
- 30 min soaking in Dentasept 3H rapid for decontamination;
- Rinsing by ultrasound;
- Cleaning with benzalkonium chloride + chloramine T + E.D.T.A betatetrasonium + Isopropyl alcohol;
- Drying at DPH21;
- Sterilization by surgical autoclave.

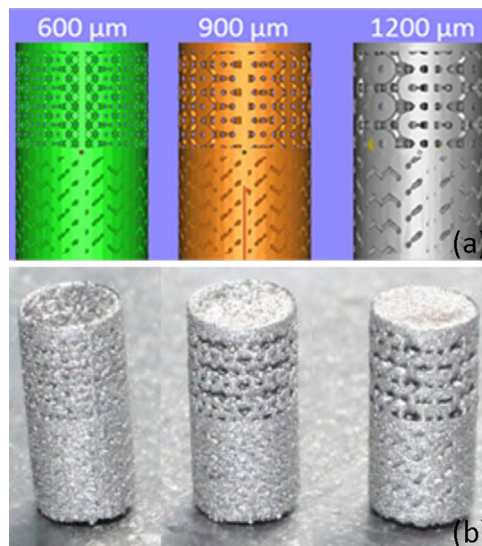


**Fig. 2.** Schemes (a) and photographs (b) of the 600, 900 or 1200  $\mu\text{m}$  lattice structure cylindrical specimens studied.

## 2.3. Characterisation techniques

### 2.3.1. Archimedes' method

The density of the specimens was determined by the hydrostatic method at Laboratoire National de Métrologie et d'Essais (LNE), the National Metrology Institute (NMI) in France. The system (Fig. 3) consists of a precision balance with a thin wire attached at the bottom end, where a suspension device is hooked. This suspension device is immersed in a container, filled with a liquid, placed beneath the balance. The balance used is of 400 g maximum weight capacity and 0.1 mg resolution. The entire setup is placed in an air-conditioned laboratory at a temperature of  $20\text{ }^{\circ}\text{C} \pm 1\text{ }^{\circ}\text{C}$  and at a humidity of  $50\% \pm 10\%$ . The LNE is Cofrac accredited 2.36 certified for density measurements with this hydrostatic method.

### 2.3.2. X-ray computed tomography

The X-ray Computed Tomography (XCT) scanning was conducted at BAM (Bundesanstalt für Materialforschung und –prüfung) in Berlin on a General Electric (GE) phoenix vltomelx L 300 computed tomograph (Fig. 4). This is a versatile system including a 300 kV microfocus X-ray tube as well as a 180 kV high-resolution nanofocus X-ray tube. The entire system is mounted on a granite-based 8-axes manipulation.

XCT scanning was performed on the cylindrical specimens with 600/900/1200  $\mu\text{m}$  diagonal cells as well as on the dental implant with 1200  $\mu\text{m}$  cells, both prior to placement and after removal from the sheep. We used the 180 kV high-resolution nanofocus X-ray tube. This tube includes a transmission target made of tungsten on diamond with a minimum focal spot size of 1  $\mu\text{m}$ . The custom bay system is also equipped with a GE  $2048 \times 2048$  pixels (200  $\mu\text{m}$  pitch) 14-bit amorphous silicon flat panel detector.

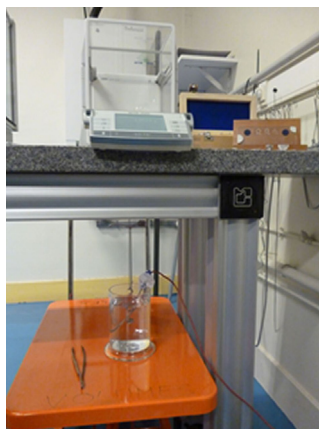


**Fig. 3.** Photograph of set-up used to measure the density of the studied parts.

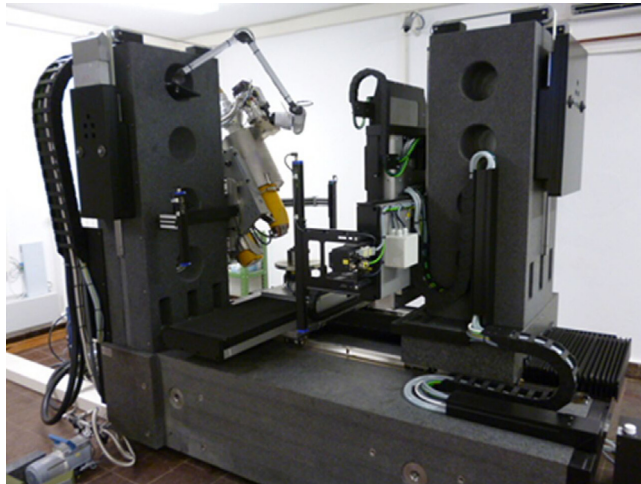


**Fig. 4.** Photograph of the X-ray computed tomograph used to characterize the studied parts (GE phoenix vltomelx L 300 computed tomograph).

The acquisitions as well as the reconstruction after the scan were performed with the phoenix datoslx GE software.

Finally, the visualisation as well as the analysis of the 3D data sets was carried out with the commercial software Avizo. This software enables exploration of the reconstructed 3D images, their segmentation, and their quantitative analysis.

### 3. Methods

#### 3.1. Sheep surgery

The surgical operations enabling to place and to remove the implants into the sheep have been approved by the French ministry of research after ethical evaluation by the facility ethical committee. These operations were performed by a surgeon assisted by a technician at the biomedical research centre of the national veterinary school of Alfort in France (Centre de Recherche BioMedicale –CRBM- de l'Ecole Nationale Vétérinaire d'Alfort). The centre has a dedicated operating room for both large and small animals. Prior to the operation, the sheep underwent a complete veterinary examination and then an anaesthesia. The anesthetic and analgesic protocol performed by an anaesthetist implied the following steps:

1. Premedication by intravenous injection of a mixture of Ketamine (6 mg/kg) and Diazepam (0.5 mg/kg);
2. Intubation with an endo-tracheal probe of 9 mm internal diameter;
3. Connection to respirator with maintenance of anaesthesia by inhalation of 2.5% Isoflurane in an air/oxygen mixture with 60% O<sub>2</sub>;
4. Analgesia: IV injection of Morphine (0.1 mg/kg);



5. NSAIDs: IM injection of Meloxicam (0.4 mg/kg);
6. Antibiotic: IM injection of 0.15 ml/kg of PeniDHS (combination of Penicillin + Streptomycin).

After its anaesthesia, the sheep's leg were shorn and brushed with chlorhexidine. The positioning and the drilling of the implants followed a strict protocol and made use of dental implantology equipment.

The euthanasia of the sheep, after eight weeks, was made by premedication by intravenous injection of a mixture of Ketamine (6 mg/kg) and Diazepam (0.5 mg/kg) followed by an injection IV of 20 ml of Pentobarbital 18%.

The parts remain into the sheep for two months as this duration corresponds to the classic practice, if we aim at highlighting bone integration of implants (as opposed to functional and medical performance).

### ***3.1.1. Surgical steps of the implants and cylindrical specimen's placement***

The surgical approach of the tibia was performed by tilting the periosteum. The procedure for the implants and the cylindrical specimens' placement were different. Since the implants are provided with a thread, they were screwed into the bone whereas the cylindrical specimens were placed in a bone cavity previously drilled at the right dimensions. Concerning the cylindrical specimens, since the cortical bone of the sheep tibia is not thick enough only the diagonal cells were immersed in the cortical bone whereas the diamond structure was essentially buried in the less bone-forming medullary. Hence, it was only possible to study the diagonal cells thereafter. As said earlier, the cylinders are vertically separated by a partition. Some blood, taken with a syringe from the sheep, was injected in one of the two zones before surgical placement. This zone was labelled in order to be identified. A good impregnation of the blood was observed. Finally, at the end of the surgery the periosteum was closed on the surgical site.

### ***3.1.2. Chirurgical steps of the implants and cylindrical specimen's removal***

For the removal of both dental implants and cylindrical specimens, the surgical site was taken over by the same approach. A visual inspection of this surgical site was carried out and compared to the immediate aspect after the implants' and specimens' placement (Fig. 5). Then the bone parts including the implants and the cylindrical specimens were sliced and immediately frozen at  $-18^{\circ}\text{C}$ . Finally, the parts were transferred in dry ice to the BAM in Berlin where they were kept frozen at  $-18^{\circ}\text{C}$  before the XCT characterizations.



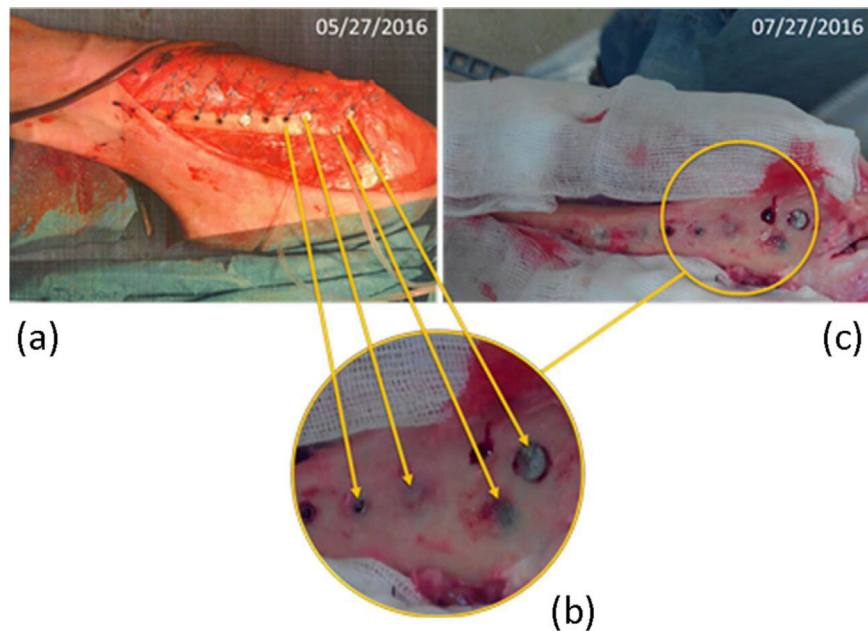


**Fig. 5.** Photographs after installation (a) and just before removal (c) of parts (dental implants and cylinder parts). (b) Zoom of photograph (c).

### 3.2. Implant production

A dedicated software, Magics, enabled the design of the theoretical dental implants and the cylindrical specimens (Computer-aided design, CAD). It also enabled calculation on the lattice structure.

Titanium scaffold cylindrical specimens and dental implants used in this study were fabricated with a powder bed fusion AM technology (SLM125<sup>HL</sup>, SLM-Solutions, Germany) (Fig. 6). The maximum build capacity of such AM machine is 125 × 125 × 125 mm.

The powder used is a titanium alloy (Ti6Al4 V, LPW, United Kingdom) with particle sizes in the range of 25–45 μm. The implants were manufactured layer-by-layer by an Yb (Ytterbium) fiber laser system, operating in an argon controlled atmosphere, using a wavelength of 1054 nm with a continuous power of 200 W at a scanning rate of 7 m/s. The laser spot size was assumed to be 0.1 mm during processing (provider's data). After each laser scan, a re-coater blade performed a double pass in the AM chamber in order to level and to homogenize the powder bed. Thus the larger particles were eliminated. The other process parameters are given in Table 1.

The dental implants and the cylindrical specimens were manufactured during the same AM process.



**Fig. 6.** Photograph of the additive manufacturing machine used to fabricate the studied parts. Selective Laser Melting (SLM) process, model 125<sup>HL</sup>, commercialized by SLM Solutions GmbH.

### 3.3. Characterisation techniques

#### 3.3.1. Archimedes' method

The density of the 600/900/1200  $\mu\text{m}$  cylindrical specimens was measured, prior to placement into the sheep (Table 2). In order to decrease the measurement uncertainty, 3 or 4 identical samples (same process of fabrication) were measured simultaneously (when available). These measurements were also performed on individual specimens in order to compare the results (Table 2). Besides, hydrofluoric acid (HF 0.5%) cleaning of the particles adhering to the structure after manufacture had been attempted (17 min in an ultrasonic tank followed by a tap water rinsing). In order to check the effect of acid, the density of a 900  $\mu\text{m}$  specimen that had undergone such treatment was also measured (Table 2).

**Table 1.** Process parameters used for scaffold fabrication.

Parameter	Symbol	Cell size in CAD model ( $\mu\text{m}$ )		
		600	900	1200
Laser current (mA)	I	1700	1700	1700
Laser Power (W)	P	80	100	100
Exposure time ( $\mu\text{s}$ )	et	40	40	40
Point distance ( $\mu\text{m}$ )	pd	15	15	20
Hatch spacing ( $\mu\text{m}$ )	h	46	48	52
Scanning speed (mm/s)	v	311	311	311
Layer thickness ( $\mu\text{m}$ )	t	30	30	30
Energy density ( $\text{J}/\text{mm}^3$ )	E	186	223	206

**Table 2.** Density, volume and percentage of metal measurements and associated uncertainty (U stands for extended uncertainty,  $k = 2$ ) using an Archimedes' method. "AC" stands for acid cleaning.

Sample reference	Mass (mg)	U ( $k = 2$ ) (mg)	Volume ( $\text{mm}^3$ )	U ( $k = 2$ ) ( $\text{mm}^3$ )	Density ( $\text{kg}/\text{m}^3$ )	U ( $k = 2$ ) ( $\text{kg}/\text{m}^3$ )	Percentage of metal (%)
E1 to E3–600 $\mu\text{m}$	3268.4	0.4	257	1	4 240.0	17.0	83
E1–900 $\mu\text{m}$	1021.6	0.4	241	1	4 239.0	18.0	78
E1 to E4–900 $\mu\text{m}$	4104.0	0.4	243.5	1.4	4 212.0	18.0	79
AC–900 $\mu\text{m}$	1095.4	0.4	354	1	3 092.0	12.0	115
E1–1200 $\mu\text{m}$	974.0	0.4	228	1	4 264.0	19.0	74
E1 to E3–1200 $\mu\text{m}$	2914.9	0.4	226	1.1	4 300.0	19.0	73

The classical principle of the hydrostatic method involves measuring the apparent mass of the sample in air, then in twice-distilled water to deduce its density. However in the case of lattice structures, with water, bubbles form at the air-lattice interface preventing the water to penetrate deep inside the lattice because the surface tension of water is too high ( $72.8 \cdot 10^{-3} \text{ N}\cdot\text{m}^{-1}$  at  $20^\circ\text{C}$ ). In order to avoid this phenomenon, which distorts the measurements, absolute ethanol was used. In that case, a good penetration of the liquid into the lattice structure was observed as the surface tension of alcohol ( $22.27 \cdot 10^{-3} \text{ N}\cdot\text{m}^{-1}$  at  $20^\circ\text{C}$ ) is much lower than water, preventing bubbles to disturb the measurement.

The samples were placed in the  $20^\circ\text{C}$  air-conditioned laboratory one day before measurements. So its temperature is assumed to be  $T_0 = 20^\circ\text{C}$ . Then the below operating mode was followed:

- 1) The balance was tared to zero.
- 2) Weighing in air ( $P_a$ ): the sample was placed on the balance and compared with mass standards according to Borda's double-substitution method.
- 3) The density of air ( $\rho_a$ ) was calculated taking into account the temperature ( $T_a$ ), the pressure and the humidity in the laboratory during measurements of the sample in air.
- 4) The sample was removed from the balance.
- 5) An eventual derivation of the tare was checked. If a derivation is observed the weighing is done again.
- 6) The balance is tared to zero
- 7) Weighing in absolute ethanol ( $P_e$ ): the sample was placed in the absolute ethanol on the suspension device. Once the sample and the temperature were stabilised, the mass of the sample was compared with mass standards placed on the weighing pan according to Borda's double-substitution method. This

comparison in absolute ethanol was carried out twice. In between each measurement an eventual derivation of the tare was checked and then the balance is tared to zero if no derivation is observed.

- 8) The temperature of the absolute ethanol inside the container was taken ( $T_l$ ) in order to take into account the variation of temperatures on the density of alcohol. Indeed, the density of the ethanol ( $\rho_{l,T_0}$ ) was preliminarily evaluated by a pycnometric method at the reference temperature of  $T_0 = 20\text{ }^\circ\text{C}$ .
- 9) The density of air ( $\rho_{a,l}$ ) was calculated taking into account the temperature ( $T_a$ ), the pressure and the humidity in the laboratory during measurements of the sample in ethanol.
- 10) Weighing in air ( $P_a$ ): the sample was placed for the second time on the balance and compared with mass standards according to Borda's double-substitution method.
- 11) The final result ( $\rho$ ) is expressed as the mean of the two measurements carried out using the relations (1) and (2):

$$\rho = \frac{A_a}{A_a - A_l} \{ \rho_{l,T_0} [1 + C_l(T_l - T_0)] [1 + C_s(T_l - T_0)] - \rho_a [1 + C_s(T_a - T_0)] \} + \rho_a [1 + C_s(T_a - T_0)] \quad (1)$$

where:

$$A_a = P_a \left( 1 - \frac{\rho_a}{\rho_e} \right)$$

and

$$A_l = P_l \left( 1 - \frac{\rho_{a,l}}{\rho_e} \right) \quad (2)$$

with  $C_l$  and  $C_s$  the thermal expansion coefficient of the liquid and of the sample respectively and  $\rho_e = 8000\text{ kg.m}^{-3}$ , the conventional value of the density of the standards.

This equation takes into account the air buoyancy correction.

The expanded uncertainty on measurement is calculated using a coverage factor  $k = 2$ , taking into account the following sources of uncertainty:

- balance;
- mass standards;
- comparisons with mass standards;
- density of the water;
- density of the air;
- volume expansion of the solid;

**Table 3.** Acquisition parameters according to the sample studied.

	Cylindrical specimens prior to placement into the sheep	Cylindrical specimens after removal from the sheep	Diamond dental implant prior to placement into the sheep	Diagonal dental implant after removal from the sheep
Accelerating voltage (kV)	100	120	90	120
Current ( $\mu$ A)	120	100	170	100
Exposure time per projection (ms)	1000	1000	2000	2000
Exposure time average (s)	2	4	4	4

- reproducibility of the measurements.

Then comparing the measured volume by the hydrostatic method with the one measured with a digital calliper, the percentage of material relative to the lattice was also determined.

### 3.3.2. X-ray computed tomography

XCT scanning was performed to the cylindrical specimens with 600/900/1200  $\mu$ m diagonal cells as well as on the dental implant with 1200  $\mu$ m cells, prior to placement and after removal from the sheep. Scanning was performed using an accelerating voltage, a current, an exposure time per projection, and an average of projections depending of the studied samples as displayed in Table 3.

No filter was used. A geometrical magnification of 30 was achieved (giving an effective pixel size of 6.6  $\mu$ m) by positioning the samples close to the conical beam X-ray source (Fig. 7). 2000 up to 2500 equally spaced projections over 360° were

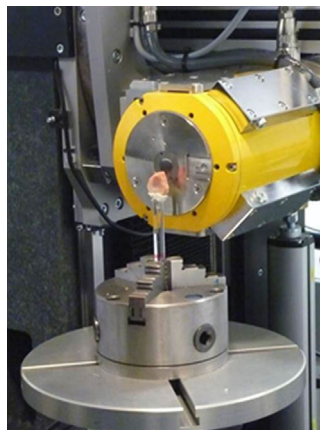


**Fig. 7.** Photograph of the position of the implant into the bone in front of the X-ray tube before XCT scanning.

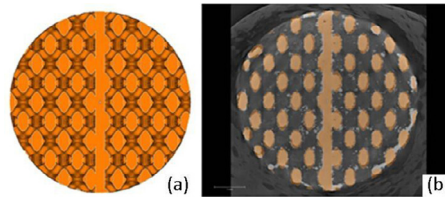


**Fig. 8.** 900  $\mu\text{m}$  cylindrical specimen CAD model slice (a) and CAD model superimposed on a XCT image slice (b) at a diagonal cell level (the scale bar indicates 1 mm).

taken, resulting in an acquisition time from 1 h to 6 h. The implants were removed from the freezer just before the acquisitions and returned to the freezer immediately after the acquisitions. They were not maintained at  $-18\text{ }^{\circ}\text{C}$  during acquisitions.

## 4. Results

### 4.1. First observation: geometric observations

A numerical image (CAD) (Fig. 8, left), of a horizontal slice of a cylindrical specimen, at the lowest of the metal proportion (i.e. where the cells are the largest), was superimposed to a XCT image (Fig. 8, right).

From these two images, using the design Magics software for the theoretical image and Avizo software for the XCT image, the measurements of the diagonal strut sizes were performed. Ten different strut size measurements, randomly distributed in each slice, were taken, and their average was taken (Table 4 for CAD and Table 5 for XCT). Table 6 gives the deviation between these two sets of results: XCT confirms the CAD model for the large cell sizes, but not for the smallest one, where deviations of about 50% were found.

### 4.2. Second observation: particle adhesion

XCT images of the dental implant (Fig. 9) and of the cylindrical specimens sliced horizontally at a diamond (Fig. 10) and a diagonal (Fig. 11) cell levels were analysed.

**Table 4.** Diagonal strut size measurements from CAD model analysis of the three different cylinders studied.

Part reference	Strut size ( $\mu\text{m}$ )										Average ( $\mu\text{m}$ )
600 $\mu\text{m}$	173	174	170	175	170	173	170	171	170	171	172
900 $\mu\text{m}$	377	382	381	324	319	363	375	317	323	356	352
1200 $\mu\text{m}$	496	495	514	496	495	493	492	496	501	459	494

**Table 5.** Diagonal strut size measurements from XCT image regarding the three different cylinders studied.

Part reference	Strut size ( $\mu\text{m}$ )										Average ( $\mu\text{m}$ )
600 $\mu\text{m}$	230	275	220	250	240	230	260	230	270	220	249
900 $\mu\text{m}$	340	310	360	425	310	350	310	360	340	325	343
1200 $\mu\text{m}$	440	440	470	440	417	480	460	440	450	490	452

Furthermore, the results concerning the mass, the volume, the density, and the percentage of metal in the cylindrical specimens, using the Archimedes' method, are given in Table 2. Table 7 and Table 8 give the deviation between the mass and volume calculated from the numerical model (CAD) and the experimental results (Archimedes' method, abbreviated Archi). The theoretical lattice volume corresponds to 45% of the theoretical dense volume.

Finally, the percentage of metal, in a given volume of diagonal cells (Fig. 12), has also been evaluated from the CAD and XCT images (Table 9).

### 4.3. Third observation: bone formation

Several XCT dental implant and cylindrical images were performed (Fig. 9 to Fig. 12). Then, in order to quantify the bone penetration (Table 10), quantitative image analysis of XCT data was performed using Avizo software. Incidentally, we notice that we indirectly checked how a dense implant would adhere to the bone tissue (osteo-integration of a continuous surface). In fact, the dental implant has dense surfaces that allowed us to conclude that the interface bone/implant is essentially defect-free (Fig. 9).

## 5. Discussion

### 5.1. First observation: geometric observations

The superposition of the CAD and XCT images (Fig. 8) enables to say that there is a good agreement between the AM design model and the part manufactured. The cells, on the CAD model, are just slightly longer than on the XCT image. This

**Table 6.** Diagonal strut size deviation between theoretical (CAD) and XCT images regarding the three different cylinders studied.

Part reference	Average CAD ( $\mu\text{m}$ )	Average XCT ( $\mu\text{m}$ )	Deviation CAD/XCT (%)
600 $\mu\text{m}$	172	249	45
900 $\mu\text{m}$	352	343	3
1200 $\mu\text{m}$	494	452	9



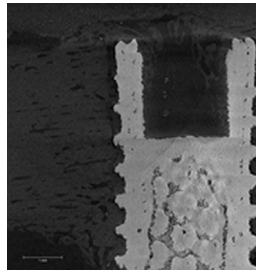


**Fig. 9.** XCT images of a dental implant (the scale bar indicates 1 mm).

good agreement is corroborated by the strut size measurements (Table 4 and Table 5) of the 900 and 1200  $\mu\text{m}$  cell cylindrical specimens, as the deviation CAD/XCT (Table 6) is only of 3 and 9% respectively. Concerning, the 600  $\mu\text{m}$  cell cylindrical specimen the deviation is much higher due to the second observation below (Table 6).

## 5.2. Second observation: particle adhesion

It could be observed that individual particles were left adhering to the inner part of the dental implants (Fig. 9) and to the cylindrical specimens (Fig. 10 to Fig. 12) after fabrication. These particles obstruct the cells of the dental implants (Fig. 9) as well as, particularly, the diamond lattice structure of the cylindrical specimens (Fig. 10). Since the diamond cells of the cylindrical specimens were buried in the medullary, which is less bone-forming, we have limited our study only to the diagonal cells of the cylindrical specimens of 600, 900 and 1200  $\mu\text{m}$ .

The particle adhesion phenomenon is not so visible on mass measurement comparison CAD/Archi (Table 7) but is highlighted by volume comparison CAD/Archi (Table 8) and by percentage of metal comparison CAD/XCT (Table 9). The 600  $\mu\text{m}$  cell specimens are particularly affected by this phenomenon so one can conclude that this size of cells is too small, compared to the powder particle size in the bed of the SLM machine. Considering the 900 and 1200  $\mu\text{m}$  cell specimens, the amount of inner particles is acceptable to study the bone integration. However, we need to underline that the theoretical calculations did not take into account the

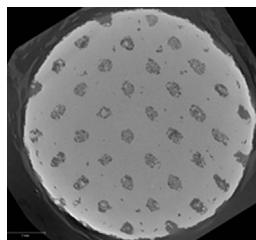


**Fig. 10.** XCT image of a 1200  $\mu\text{m}$  cylindrical specimen horizontally sliced at a diamond cell (the scale bar indicates 1 mm).

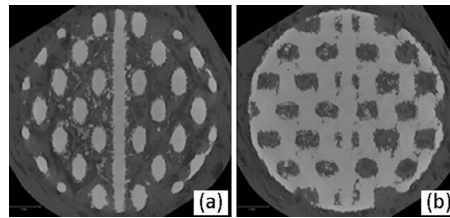


**Fig. 11.** XCT images of a 1200  $\mu\text{m}$  cylindrical specimen sliced at two different diagonal cell levels: at minimum percentage of metal (a) and at maximum percentage of metal (b) (the scale bar indicates 1 mm).

influence of the manufacturing process parameters (Table 1). These are based only on the part designs. Nevertheless, this influence is much lower than the presence of remaining infused particles.

Finally, it is clear that the acid cleaning was not effective in removing the adhering particles, at least with the used dosage (HF 0.5% during 17 min). On the contrary, it had the effect of clogging the cells. Indeed, the volume of acid cleaned specimen is higher than the one of untreated specimen (Table 8).

### 5.3. Third observation: bone formation

As is particularly highlighted by the XCT images of the dental implant (Fig. 9), there is a very good bone adhesion on the surface of the implant (bone is represented by light grey colour). This was also observed on the leg of the sheep just before removal of the dental implants and cylinder specimens (Fig. 5). This surface bone proliferation on AM titanium implants has been already observed, in human body, by Mangano [3] and Shibli [1].

Even more interestingly, the penetration of bone into the structure is clearly noticeable in the 900 and 1200  $\mu\text{m}$  diagonal cell parts of the cylindrical specimens (Fig. 11 and Fig. 12). This penetration is evenly distributed in the 900  $\mu\text{m}$  specimen (Fig. 11), but seems to decrease progressively towards the centre in the 1200  $\mu\text{m}$  specimen (Fig. 12). This is supported by the calculation of the fraction of bone in the cells. From these results, it seems that the 900  $\mu\text{m}$  size cells is more adapted to bone integration than the 1200  $\mu\text{m}$  size cells. Indeed, the percentages of

**Table 7.** Mass deviation between the theoretical (CAD) and Archimedes' method (Archi) for the three different cylinders studied.

Part reference	CAD mass (mg)	Archi mass (mg)	Deviation CAD/Archi (%)
600 $\mu\text{m}$	928.9	1089.5	17
900 $\mu\text{m}$	930.3	1021.6	10
1200 $\mu\text{m}$	913.9	974.0	7

**Table 8.** Volume deviation between the theoretical (CAD) and Archimedes' method (Archi) for the three different cylinders studied.

Part reference	CAD dense volume (mm <sup>3</sup> )	CAD lattice volume (mm <sup>3</sup> )	Archi lattice volume (mm <sup>3</sup> )	Deviation CAD/Archi (%)
600 $\mu\text{m}$	289.4	130.2	257	97
900 $\mu\text{m}$	291.3	131.1	243.5	86
1200 $\mu\text{m}$	292.2	131.5	226	72

bone occupying the space left by the metal are respectively 84% and 54% (Table 10), the rest being occupied by non-bone biological tissue. However, this lack of ossification for cells higher than 1000  $\mu\text{m}$  is may be just a question of remaining for more time into the sheep. There might be a difference with a three months study. However, even if, several specialists report the idea that the larger the cells, the higher the bone penetration, Taniguchi et al. [11] affirm that some cell sizes favour bone integration more than others.

Finally, it should be noted that blood injection into one part of the cylindrical specimens prior to the placement into the sheep bone has no notifiable effect on the bone integration.

## 6. Conclusion

For the first time to our knowledge, we have demonstrated bone integration into lattice implants additively manufactured (AM) by a selective laser melting (SLM) process, making use of a laser instead of an electron beam like in the electron beam melting (EBM) process.

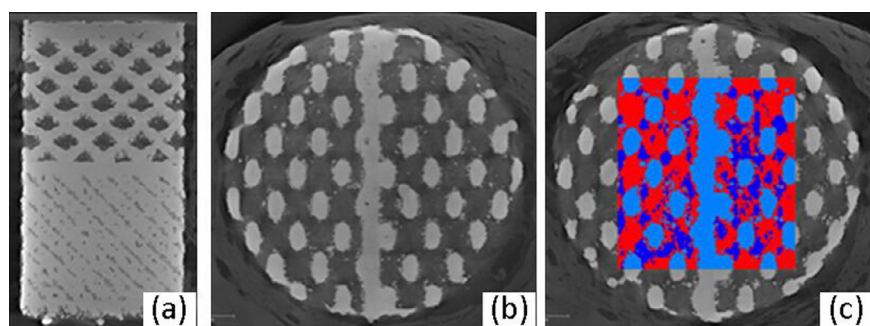


**Fig. 12.** XCT images of a 900  $\mu\text{m}$  cylindrical specimen: lateral view (a) and horizontal slices at two different diagonal cell levels (band c). The volume used, to calculate the faction of metal is displayed in colour (right) (the scale bar indicates 1 mm).

**Table 9.** Percentage of metal in a given volume with diagonal cells as given by Avizo software compared to theoretical intended initial percentage of metal in a given volume as planned by the numerical model (CAD) in the three different cylinders studied.

Part reference	CAD	XCT	Deviation CAD/XCT
600 $\mu\text{m}$	44%	78%	77%
900 $\mu\text{m}$	54%	63%	17%
1200 $\mu\text{m}$	53%	59%	11%

Several cylindrical specimens and dental implants, presenting diagonal lattice structures with different cell sizes 600, 900 and 1200  $\mu\text{m}$ , were implanted for two months in a sheep. After removal, they were studied by Archimedes' method as well as X-ray computed tomography in order to appreciate the penetration of bone into the lattice. The first method enables evaluations of the density whereas the second enables non-destructive visualisation of the inner of the structure (of both geometry and defects). We have observed that the AM parts were geometrically conform to the theoretical specifications (CAD drawing). However, several particles were left adhering to the surface of the lattice and they partly or entirely obstructed the 600  $\mu\text{m}$  cell specimen. Nevertheless, bone penetration in the 900 and 1200  $\mu\text{m}$  lattice structures was clearly visible. While we cannot exclude an influence of the implant residence time in the sheep, it seems that the 900  $\mu\text{m}$  lattice cell size is more favourable to bone penetration than the 1200  $\mu\text{m}$  lattice cell size, as the bone penetration is of 84% for 900  $\mu\text{m}$  against 54% for 1200  $\mu\text{m}$  cell structures.

These results will contribute to the acceptance of the AM technology in the medical sector as we have clearly shown that lattice structure enables better bone integration, which will be very beneficial for the patient, shortening the recovery time after surgery.

**Table 10.** Percentage of metal in a given volume with diagonal cells as given by Avizo software compared to percentage of bone and percentage of non-bone biological tissue in the two of the studied cylinders. Last two columns, global percentages of bone and non-bone biological tissue.

Part reference	metal	bone	non-bone biological tissue	bone occupying the space left by the metal	non-bone biological tissue occupying the space left by the metal
900 $\mu\text{m}$	63%	31%	6%	84%	16%
1200 $\mu\text{m}$	59%	22%	19%	54%	46%

The next step will be to improve the lattice structure cleaning after manufacturing in order to eliminate the adhering particles, and to consider a medical study performing a statistical analysis involving several animals.

## Declarations

### Author contribution statement

A-F. Obaton: Conceived and designed the experiments; Performed the experiments; Analyzed and interpreted the data; Contributed reagents, materials, analysis tools or data; Wrote the paper.

J. Fain: Conceived and designed the experiments; Analyzed and interpreted the data; Contributed reagents, materials, analysis tools or data; Wrote the paper.

M. Djemaï: Conceived and designed the experiments; Performed the experiments; Contributed reagents, materials, analysis tools or data.

D. Meinel, E. Mahé and B. Lécuelle: Performed the experiments.

F. Léonard: Analyzed and interpreted the data.

J-J. Fouchet: Conceived and designed the experiments.

G. Bruno: Wrote the paper.

### Funding statement

This work was supported by the EMPIR programme, co-financed by the Participating States and from the European Union's Horizon 2020 research and innovation programme.

### Competing interest statement

The authors declare no conflict of interest.

### Additional information

No additional information is available for this paper.

## References

- [1] J.A. Shibli, S. Grassi, A. Piattelli, G.E. Pecora, D.S. Ferrari, T. Onuma, S. d'Avila, P.G. Coelho, R. Barros, G. Iezzi, Histomorphometric Evaluation of Direct Laser Metal Forming (DLMF) Implant Surface in the Type IV Bone: A Controlled Study in Human Jaw, Poseido. 1 (3) (2013) 45–52.

- [2] W. Peng, L. Xu, J. You, L. Fang, Q. Zhan, Selective laser melting of titanium alloy enables osseointegration of porous multi-rooted implants in a rabbit model, *BioMed Eng Online* 15 (2016) 85.
- [3] C. Mangano, A. Piattelli, F. Mangano, F. Rustichelli, J.A. Shibli, G. Iezzi, A. Giuliani, Histological and synchrotron radiation-based computed microtomography study of 2 human-retrieved direct laser metal formed titanium implants, *Implant Dent.* 22 (2) (April 2013) 175–181.
- [4] R.M. Sherekar, A. Pawar, P. Bheda, Manufacturing of biocompatible TiAl6V4 alloy in direct metal laser sintering for anatomical implants, *American Journal of Materials Science and Application* 2 (5) (2014) 69–75.
- [5] Additive manufacturing-General principles-Part 2:Overview of process categories and feedstock, ISO/DIS 17296-2, (24 Jun 2014) .
- [6] R. Wauthle, S.M. Ahmadi, S. Amin Yavari, M. Mulier, A.A. Zadpoor, H. Weinans, J. Van Humbeeck, J.P. Kruth, J. Schrooten, Revival of Pure Titanium for Dynamically Loaded Porous Implants Using Additive Manufacturing, *Mater. Sci. Eng. C.* 54 (1 September 2015) 94–100.
- [7] R. Wauthle, J. van der Stok, S. Amin Yavari, J. Van Humbeeck, J.P. Kruth, A.A. Zadpoor, H. Weinans, M. Mulier, J. Schrooten, Additively manufactured porous tantalum implants, *Acta Biomater.* 14 (2015) 217–225.
- [8] A. Palmquist, F.A. Shah, L. Emanuelsson, O. Omar, F. Suska, A technique for evaluating bone ingrowth into 3D printed, porous Ti6Al4 V implants accurately using X-ray micro-computed tomography and histomorphometry, *Micron* 94 (2017) 1–8.
- [9] G. Li, L. Wang, W. Pa, F. Yang, W. Jiang, X. Wu, X. Kong, K. Dai, Y. Hao, In vitro and in vivo study of additive manufactured porous Ti6Al4 V scaffolds for repairing bone defects, *Nature* (2016). [www.nature.com/scientificreports](http://www.nature.com/scientificreports).
- [10] M. Dejmaï, J.-J. Fouchet, Ensemble constitué d'un implant dentaire et d'un élément de fixation autobloquant à structures poreuses hétérogènes et son procédé de fabrication 3. 036. 945-(A1)-[15 01133], (2 Jun 2015) .
- [11] N. Taniguchi, S. Fujibayashi, M. Takemoto, K. Sasaki, B. Otsuki, T. Nakamura, T. Matsushita, T. Kokubo, S. Matsuda, Effect of pore size on bone ingrowth into porous titanium implants fabricated by additive manufacturing: An in vivo experiment, *Mater. Sci. Eng. C.* 59 (2016) 690–701.